Large Scale Graphene/Hexagonal Boron Nitride Heterostructure for Tunable Plasmonics

*Kai Zhang, Fung Ling Yap, Kun Li, Chang Tai Ng, Lin Jun Li, and Kian Ping Loh**

Vertical integration of hexagonal boron nitride (*h*-BN) and graphene for the fabrication of vertical field-effect transistors or tunneling diodes has stimulated intense interest recently due to the enhanced performance offered by combining an ultrathin dielectric with a semi-metallic system. Wafer scale fabrication and processing of these heterostructures is needed to make large scale integrated circuitry. In this work, by using remote discharged, radio-frequency plasma chemical vapor deposition, wafer scale, high quality few layer *h*-BN films are successfully grown. By using few layer *h*-BN films as top gate dielectric material, the plasmon energy of graphene can be tuned by electrostatic doping. An array of graphene/*h*-BN vertically stacked micrometer-sized disks is fabricated by lithography and transfer techniques, and infrared spectroscopy is used to observe the modes of tunable graphene plasmonic absorption as a function of the repeating (G/*h*-BN)$_n$ units in the vertical stack. Interestingly, the plasmonic resonances can be tuned to higher frequencies with increasing layer thickness of the disks, showing that such vertical stacking provides a viable strategy to provide wide window tuning of the plasmons beyond the limitation of the monolayer.

1. Introduction

Graphene is an atomically thin semi-metal with sp^2-bonded carbon atoms arranged in a honeycomb lattice and it can be patterned by various techniques into ribbons or disks.[1–3] Hexagonal boron-nitride (*h*-BN) is the insulating analog of graphene with alternating boron and nitrogen atoms in the honeycomb lattice.[4] The lattice mismatch between graphene and *h*-BN allows planar or vertical interfacing of atomically thin graphene and *h*-BN sheets to form integrated circuits with lateral transistors, vertical field effect transistors and tunneling diode.[5–10] High ON-OFF switching ratio can be achieved at room temperature using *h*-BN as vertical transport barrier.[8] To date, most graphene/*h*-BN heterostructures were fabricated using micrometer-sized, mechanically exfoliated graphene and *h*-BN layers flakes. To achieve scaling in device fabrication, the growth of wafer-size, few-layer *h*-BN films is necessary. In addition, few-layer *h*-BN films with appropriate thickness of ≈1 to 2 nm can provide more effective electrical insulation and also more effective shielding of the impurity scattering from the substrate than monolayer *h*-BN.[8] A commonly employed method to grow *h*-BN film is based on thermal decomposition of BN precursors on transition metals.[11–22] *h*-BN films obtained by this method are typically monolayer films since the growth is self-limited after the completion of the first layer.[11–16,20–22] Growing thicker films is non-trivial as usually non-homogenous and rough films result.[17–19]

Here, wafer scale, few-layer *h*-BN films were successfully grown by employing a remote-discharged radio-frequency plasma beam to generate pre-dissociated borazine precursors. We show here that the as-grown *h*-BN films can be used as top gate dielectric material and also stacked and patterned with graphene films to form (graphene/h-BN)*n* disks arrays. Interestingly, the plasmonic resonances can be tuned to higher frequencies with increasing layer thickness of the disks, showing that such vertical stacking provides a viable strategy to provide wide window tuning of the plasmons beyond the limitation of the monolayer.

Dr. K. Zhang, C. T. Ng, Dr. L. J. Li, Prof. K. P. Loh
Graphene Research Centre and Department of Chemistry
National University of Singapore
3 Science Drive 3, 117543, Singapore
E-mail: chmlohkp@nus.edu.sg
Dr. F. L. Yap
Institute of Materials Research and Engineering (IMRE)
Agency for Science, Technology and Research (A*STAR)
3 Research Link, 117602, Singapore
Dr. K. Li
Advanced Nanofabrication
Imaging and Characterization Core Lab
King Abdullah University of Science and Technology
Thuwal, 239955, Kingdom of Saudi Arabia

DOI: 10.1002/adfm.201302009

2. Results and Discussion

The synthesis of *h*-BN films was carried out using a remote-discharghed atom beam source. *h*-BN films were grown on 2-inch Cu (500 nm)/SiO_2/Si wafers by using borazine ($B_3N_3H_6$) as the precursor (**Figure 1**a; see detailed growth methods in the Experimental Section). Under plasma discharge, the borazine precursors are pre-dissociated into radicals. As a result, the subsequent growth of *h*-BN can be very efficient, typically, only ≈3 min of deposition time is needed to grow a continuous, few-layer *h*-BN film. The substrate is held at a relatively lower temperature of ≈800 °C compared to ≈1000 °C in thermal CVD methods. After growth, *h*-BN films were coated with poly(methyl methacrylate) (PMMA) and transferred onto

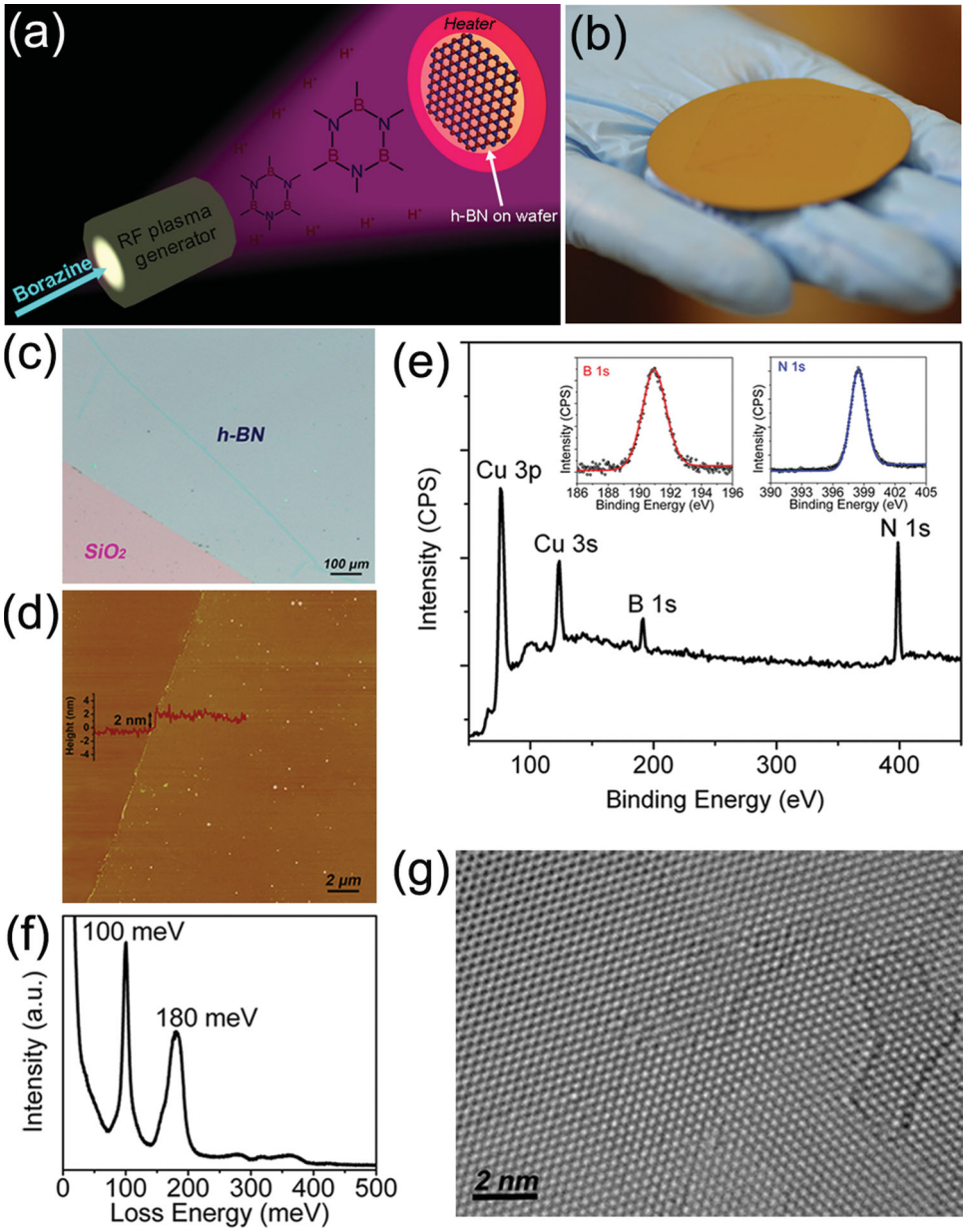

Figure 1. a) Schematic diagram of *h*-BN synthesis using a remote-discharged RF plasma beam. b) Photograph of a wafer-scale *h*-BN film. c) Optical microscopy image of the uniform *h*-BN film on SiO_2-coated silicon. d) AFM image of *h*-BN film. The line-scan profile along the edge indicates that *h*-BN film has a thickness of around 2 nm. e) XPS survey of the *h*-BN film grown on Cu-coated (500 nm)/SiO_2/Si wafer. The inset shows B 1*s* and N 1*s* XPS spectra, respectively. f) HREELS spectrum of as-grown *h*-BN film. g) Atomic resolution HRTEM image of the *h*-BN film.

desired substrates by the conventional float-transfer method.[23] Figure 1b shows the photographic image of a large scale *h*-BN film on a 2-inch silicon wafer with 285 nm thick SiO_2. A typical optical microscope image (Figure 1c) shows that the film is homogeneous with almost no color variation except for the folded region near the edge. Atomic force microscopy (AFM) characterization along the edge of the film indicates a thickness of ≈2 nm (Figure 1d), which corresponds to a few-layer *h*-BN film of 2–4 layers.[23]

Figure 1e shows the XPS spectra of the as-grown *h*-BN film on Cu (500 nm)/SiO_2/Si wafer. The wide scan spectrum indicates pure BN phase on copper without any carbon or oxygen contamination. The binding energies of B 1*s* and N 1*s* from the XPS measurement (inset in Figure 1e), located at 190.95 eV and 398.45 eV, respectively, correspond well to the reported peak positions for *h*-BN film.[17,18] The B/N ratio from the XPS characterization is calculated to be 1.005, which is consistent with the elemental stoichiometry of *h*-BN. The high resolution electron energy loss (HREELS) spectrum of the as-grown *h*-BN film shows strong peaks at 100 meV and 180 meV (as shown in Figure 1f), which are assigned to the out-of-plane and in-plane optical phonons of *h*-BN, respectively.

Edge phonon peak related to defects or edges of islands is usually located around 90 meV in the HREELS spectra, as has been observed in the case of isolated *h*-BN islands. The absence of edge phonons thus indicates the presence of a continuous *h*-BN film.[24] The hexagonal phase of the grown BN films is also evidenced by the Fourier transform infrared spectroscopy (FTIR) with strong adsorption bands centered at 813.8 cm^{-1} and 1382.7 cm^{-1}, which corresponds to the B–N–B out of plane bending vibration and B–N in plane stretching vibration of *h*-BN (Figure S1, Supporting Information).[17] The UV-Vis spectrum shows an absorption peak at ≈202 nm assignable to the interband transition and the derived optical band gap of 5.47 eV agrees well with the predicted gap of h-BN (Figure S2, Supporting Information).[18] The high resolution transmission electron microscopy (HRTEM) image of the *h*-BN film transferred on TEM grid reveals the distinctive hexagonal lattice structure of *h*-BN (Figure 1g). It can be seen that domains due to both bernal and turbostatic stacking coexist (Figure S3, Supporting Information). The "three-for-six" triangular atomic patterns of bernal stacked *h*-BN layers and the 6-fold honeycomb structure with moiré superstructure arising from incommensurately stacked *h*-BN domains are observed in the atomically resolved images.[25–27]

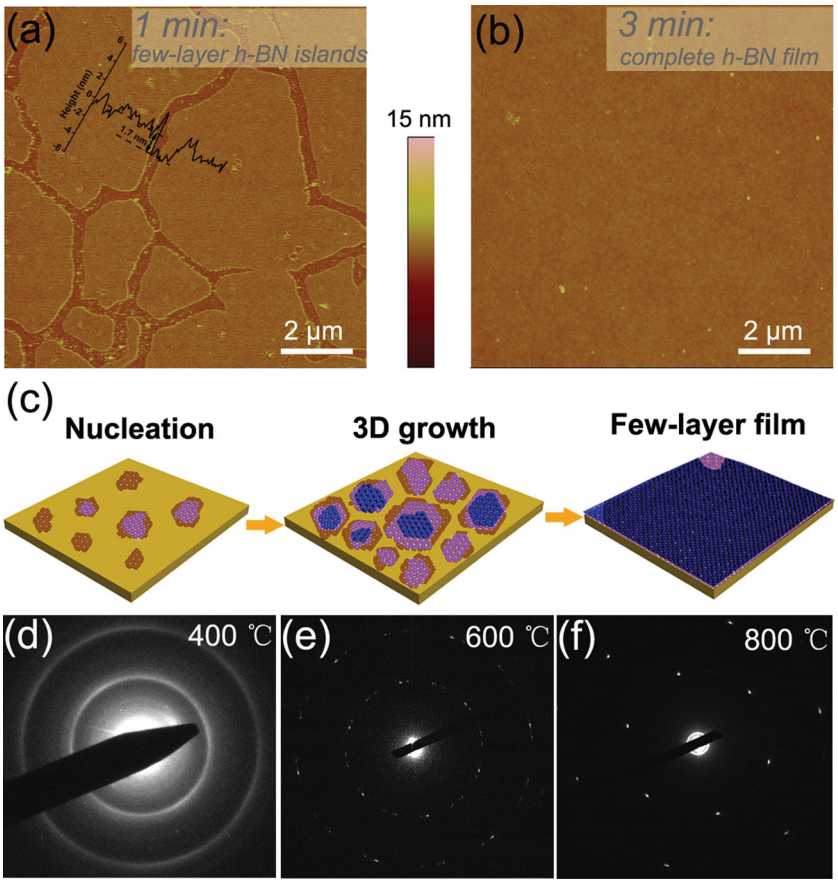

Figure 2. a) AFM image of *h*-BN islands after 1 min of growth time. Insert line-scan characterization shows the thickness of the island is ≈1.7 nm, which corresponds to thickness of 2–3 layers. b) AFM image of a continuous *h*-BN film after 3 min of growth time. The RMS of the film is ≈0.4 nm. c) Schematic illustration of the time-evolution growth of few-layer *h*-BN film by RF plasma CVD. d–f) SAED patterns of the *h*-BN films synthesized at d) 400, e) 600, and f) 800 °C, respectively.

Figure 2a,b shows the AFM images of the *h*-BN films with different growth time. Few-layer islands with thickness of ≈1.7 nm (line-scan profile shown in insert of Figure 2a), corresponding to 2–3 layers of *h*-BN were formed before merging into a complete film (Figure 2a, growth time of 1 min).[23] As shown in Figure 2b, continuous film with a root-mean-square (RMS) of 0.4 nm, without any breaks or large thickness fluctuation can be obtained after a growth time of 3 min. The results show that coalescence of *h*-BN islands (schematically illustrated in Figure 2c) allows the synthesis of uniform few-layer *h*-BN films compared to the self-limited monolayer films by thermal CVD methods.[11–16,20–22] The kinetic barrier for the growth of few-layer *h*-BN film is reduced compared to the conventional thermal CVD methods due to pre-dissociation of precursors by the plasma. The plasma activation of borazine produces gas phase radicals which impinge on the substrate to form growth nuclei. The adatom–adatom interaction among the BN radicals is particularly strong, leading to formation of 3D clusters. In a continuous flux of these radicals, a high density of these 3D clusters aggregate to form islands, which merge to form a complete film. Interrupting the growth after a short interval ensures that coarsening beyond a few layers does not occur.

Figure 2d–f indicates the evolution of crystallinity of the *h*-BN films under different growth temperatures. It demonstrates that well crystallized *h*-BN films can be grown at 600–800 °C compared to ≈1000 °C in thermal CVD methods.

The synthesized few–layer *h*-BN film shows excellent insulating characteristic with measured sheet resistance of ≈2 TΩ per square and a dielectric breakdown electric field of 5 MV cm^{-1} (Figure S4, Supporting Information). The *h*-BN film is also highly transparent with only ≈0.4% optical absorption over wavelength range of 250–800 nm (Figure S5, Supporting Information). Exploiting these advantages, we applied the few-layer *h*-BN films as a top gate dielectric layer for the electrostatic tuning of plasmon resonance in graphene. **Figure 3**a illustrates the schematic diagram of the device. Monolayer graphene grown by CVD was used as transparent gate electrode. Patterned graphene gratings (width: 2 μm; spacing: 2 μm) were used as the active layers for generating plasmons. The graphene gratings were grounded, and bias voltage was applied through top graphene layer connected to a gold pad. The graphene gratings in the heterostructure device were fabricated by nanoimprinting followed by O_2 plasma etching. The gate electrode consisted of the dielectric *h*-BN film and a graphene layer, which were transferrred onto the graphene gratings sequentially by the conventional float-transfer method. The gold pad electrodes were deposited by thermal evaporation and defined with a mask.

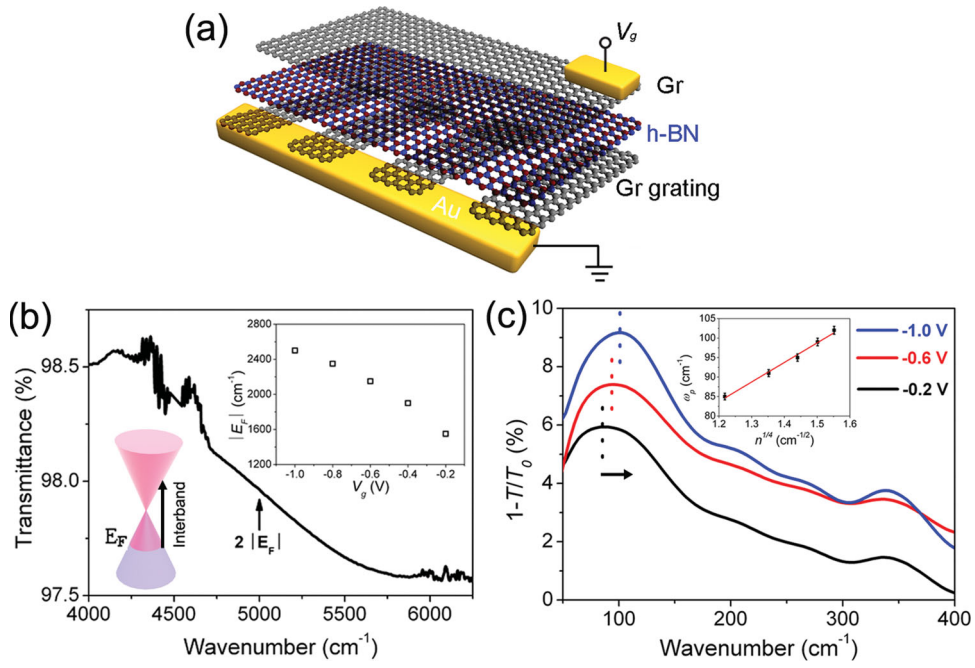

Figure 3. a) Schematic diagram of the device structure for electrostatic tuning of plasmons in a graphene/*h*-BN heterostructure. Graphene is used as the gate electrode, *h*-BN is used as the dielectric gate and patterned graphene strips are active layers for plasmons. b) Characterization of Fermi level after electrostatic doping. Insert shows the variation of Fermi level of graphene with applied gate voltage. c) Plasmon resonance shift triggered by gate voltage. Insert is the dependence of resonance frequency on carrier density, which shows linear relationship of ω_p and $n^{1/4}$.

The carrier density of the graphene layer can be actively controlled by electrostatic doping when applying gate voltage. The Fermi level of the active graphene layer was characterized by FTIR in mid-IR range. For interband transition in graphene (as shown in insert of Figure 3b), there is an increase of absorption when $h\nu > 2|E_F|$.[28,29] With –1 V gate voltage, the $2|E_F|$ of the active graphene layer is located at around 5000 cm^{-1}, which can be determined from the half maximum of the deep peak in transmittance spectrum (Figure 3b).[29] The carrier density n can be described by $n = (|E_F|/\hbar v_F)^2/\pi$,[30] for example, for –1 V gate voltage, it corresponds to $n \approx 6 \times 10^{12}$ cm^{-2}. In this way, the carrier density of the active graphene layer can be electrostatically gated. Insert in Figure 3b shows the variation of carrier density with the gate voltage from –0.2 V to –1 V. With the incident light polarized perpendicular to the graphene gratings in the device, a sharp plasmonic resonance peak was obtained in the far-IR. By controlling the gate voltage, the plasmonic resonance frequency ω_p can be tuned by electrostatic doping. Figure 3c presents the extinction spectra, $1 - T/T_0$, of the heterostructure device under various gate voltages, where T and T_0 are the transmission through the sample and bare reference substrate, respectively. As shown in Figure 3c, the plasmonic resonance upshifts from 85 cm^{-1} to 102 cm^{-1} when gate voltage is changed from –0.2 V to –1 V. The plot showing the dependence of the plasmon resonance frequency with carrier density (insert in Figure 3c) reveals an $n^{1/4}$ power-law dependence which is characteristic of two-dimensional massless Dirac electrons in graphene.[30]

The plasmon frequency of single-layer graphene has a significantly weaker carrier dependence compared to two dimensional electron gas (2DEG), showing a power law dependence of $n^{1/4}$ versus $n^{1/2}$ for 2DEG. Such weak dependence on carrier density of the plasmon in monolayer graphene significantly limits its tunability. A much stronger carrier dependence of the plasmon can be achieved by distributing the Dirac fermions in single layer graphene into multiple layers of closely spaced stack, where a significant upshift of the resonance frequency can be produced through dipole–dipole interactions of the carriers. Here, we take advantage of the strong insulating property and ultrathin nature of the *h*-BN to construct the graphene/*h*-BN vertical stacks. **Figure 4**a shows the scheme to make multilayers of stacked graphene and *h*-BN heterostructures. Figure 4b shows the actual multiple stacked (graphene/*h*-BN/graphene)*n* film supported on a 1 cm square quartz substrates where the color of the samples deepens with the increase of graphene layers inside the stacks. The thickness dependence of the IR-absorption of these heterostructures can be characterized by FTIR when the film is assembled on an intrinsic silicon substrate. In the mid-IR range, the intensity of absorptions increased with the layer number of graphene. This is also accompanied by an increasingly strong and sharp peak at 1370 cm^{-1}, which corresponds to *B*–*N* in plane stretching vibration of *h*-BN (Figure 4c).[17] In the far-IR range (Figure 4d), the transmittance of monolayer graphene decreases to ≈80% when reaching the lower wavenumber of 50 cm^{-1} due to far-IR shielding effect of graphene layers. With increasing graphene layers in the heterostructure stacks, the far-IR transmittance of the samples also decreases gradually. The transmittance T can be well fitted by Fresnel's equation $T = |1+\sigma(\omega)/(2c\varepsilon_0)|^{-2}$, where $\sigma(\omega)$ is the optical conductivity

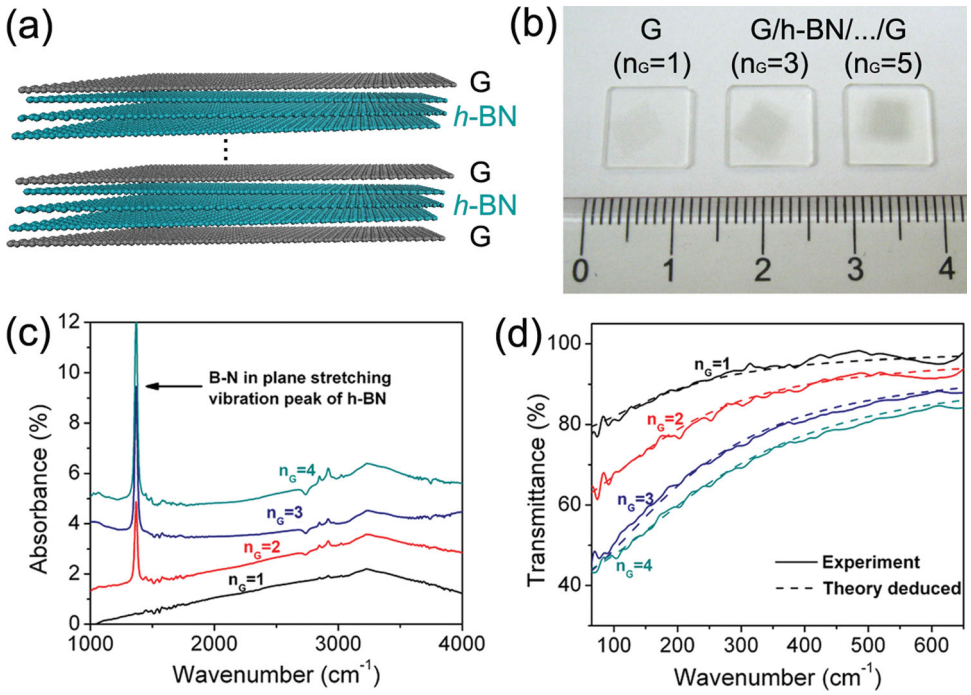

Figure 4. a) Scheme showing layer-by-layer stacking of the graphene and *h*-BN. b) Graphene/*h*-BN stacks with different layer numbers transferred on 1 cm square quartz substrates. c,d) Mid-IR and Far-IR transmittance of the graphene/*h*-BN heterostructures. The sharp peak around 1370 cm^{-1} corresponds to *B–N* in plane stretching vibration of *h*-BN.

according to $\sigma(\omega) = \sigma_0\theta(\omega\hbar - 2E_F) + i\sigma_0\frac{4E_F}{\pi\omega\hbar} - i\frac{\sigma_0}{\pi}\ln\frac{|\hbar\omega+2E_F|}{|\hbar\omega-2E_F|}$, and $\sigma_0 = \pi e^2/(2h)$ is the universal conductivity of graphene.[31] By repeating nitric acid vapor exposure to each graphene layers within the heterostructure stacks during multiple transfer, the carrier density can be increased with different layer numbers, and this is verified by the stiffening of the G band in the Raman spectra (**Figure 5**). The increase of charge carrier density with the layer number of graphene (p-doped by acid) in graphene/*h*-BN heterostructures is well evidenced by the increase of D-band peak intensity, upshift of G-band peak, and decrease of I_{2D}/I_G ratio in the Raman spectra (Figure 5a).[32,33] The carrier density n can be quantitatively correlated to the shift of G peak with increase of $\approx 1 \times 10^{12}$ cm^{-2} per 1 cm^{-1} G peak upshift for hole-doping.[33] Figure 5b shows the G-band stiffens (shifts from 1580 cm^{-1} to 1592 cm^{-1}) with increasing numbers of doped graphene layers in the graphene/h-BN heterostructure stacks. We can achieve a carrier density of 1×10^{13} cm^{-2} using a heterostructure stack that comprises four graphene layers.

The direct interaction of localized graphene plasmons with infrared light has been demonstrated previously by Yan and coworkers using a stack of graphene microdiscs spaced apart by polymer, which allowed the plasmons to be tuned through changing the dimension and thickness of the discs.[34] Similar in principle to the previous work, the variation in carrier densities due to the different stacking layers in the graphene/*h*-BN heterostructure is used as the basis to tune the plasmon resonance. In the stacks, few-layer *h*-BN film acts as an ultrathin dielectric that allows dipole–dipole coupling between the carriers in graphene layers. The graphene/*h*-BN stack was prepared and patterned by optical lithography followed by O_2 plasma etching, where each graphene layer in the heterostucture was

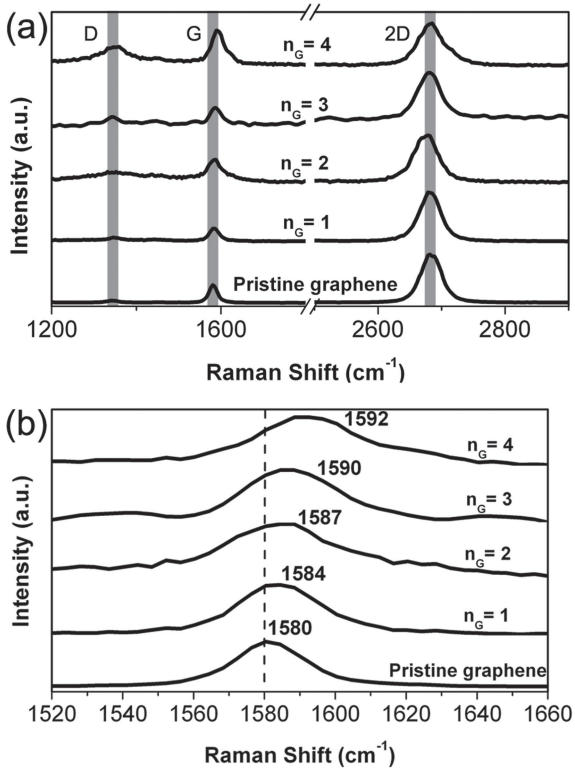

Figure 5. Increased carrier density in graphene/*h*-BN heterostructure stacks with increasing numbers of graphene layers (n_G). a) Raman spectra of the stacks with increasing n_G. The spectra were normalized by the graphene 2D peak. b) Raman G-band peak shifts with increasing n_G in the stack.

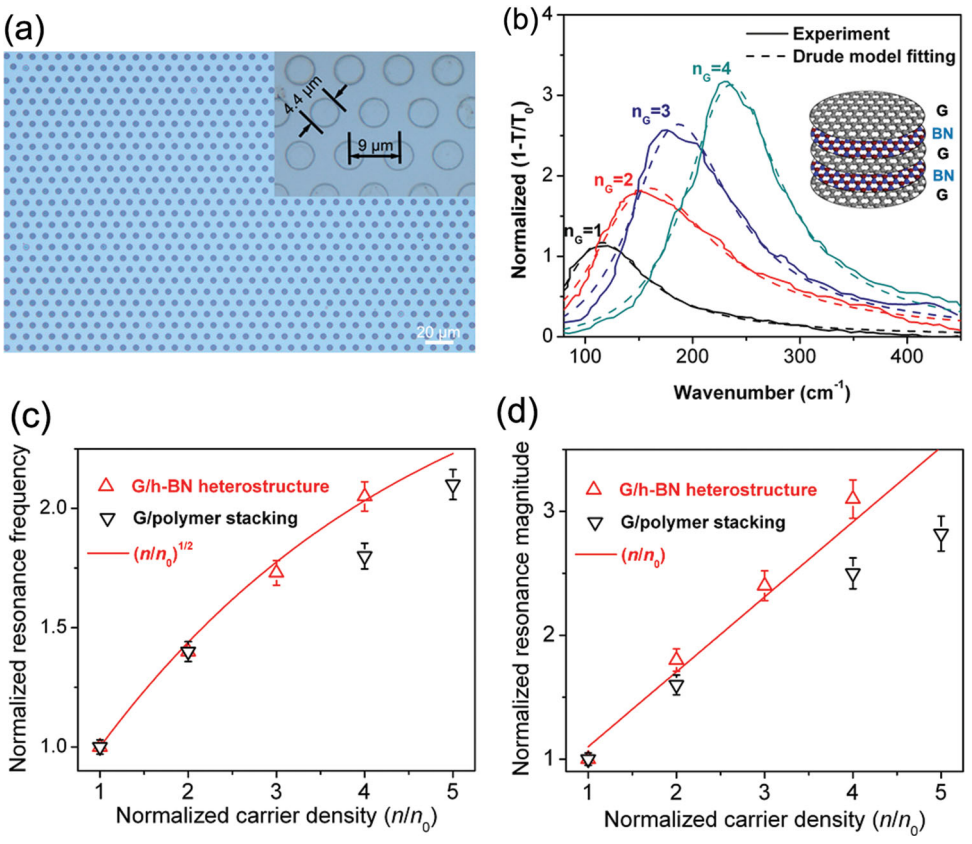

Figure 6. a) Optical image of a graphene/*h*-BN microdisk array on an intrinsic silicon substrate. Insert shows the enlarged image with dimension specifications. The diameter of the disk is 4.4 μm and the disk center to center distance is 9 μm. b) Normalized extinction spectra of the microdisk array with various graphene layer numbers (n_G). Insert shows the schematic structure of the heterostructure stacking. c,d) A larger tunability of the plasmon resonance frequency and magnitude with n_G is observed in the graphene/*h*-BN heterostructure stacks compared to the graphene/polymer stacks, the latter results are reproduced from the literature.[34] *n* and n_0 are the total carrier density of the stacks and that of a single-layer graphene, respectively. Solid lines in (c,d) are power-law scaling curves of resonance frequency (or magnitude) vs carrier density dependence.

p-doped by nitric acid vapor. **Figure 6**a shows an optical image of the microdisk patterned graphene/*h*-BN heterostructure on an intrinsic silicon substrate, which is arranged in triangular lattice with disk diameter of 4.4 μm and disk center to center distance of 9 μm. The plasmon resonance in the heterostructure is studied by FTIR in far-infrared range. Figure 6b shows the normalized extinction spectra of microdisk patterned graphene/*h*-BN heterostructures with various graphene layer numbers, where T and T_0 are the transmission through the graphene/h-BN heterostructure sample and bare intrinsic silicon substrate, respectively. The acquired spectra can be well fitted by the Drude model. We can get giant plasmon resonance tunability with the variation of the graphene layer number in the graphene/*h*-BN heterostructure stacks. The plasmon resonance frequency upshifted as large as 240 cm^{-1}, while its magnitude is enhanced by three times when the graphene layers in the heterostructure increased from one to four layers.

Due to the quantum mechanical effect, the plasmon resonance shift in the graphene/*h*-BN stack is related to the discontinuous change of the plasmon mass, $m_p = \hbar\sqrt{\pi n}/v_F$, which results in a $n^{1/2}$ carrier density dependence.[34,35] Figure 6c,d presents the dependence of normalized resonance frequency and magnitude with normalized carrier densities in the graphene/*h*-BN heterostrucutres, where, the total carrier density n in the stack increases with graphene layer number (n_0 represents the carrier density of a single-layer graphene), as described in Figure 5. The results show that the plasmon resonance frequency and magnitude follow the rule of $n^{1/2}$ and n carrier density dependence, respectively. When the graphene layer number increases from one to four layers, the plasmon resonance frequency in graphene/*h*-BN heterostructure upshifts ≈2.1 times together with 3 times enhancement of its magnitude. This is larger than the ≈1.8 times resonance shift and 2.5 times magnitude enhancement obtained in the graphene/polymer stacks shown previously.[34] The ultrathin *h*-BN film used here (≈2 nm thick) enables stronger plasmon coupling between adjacent graphene layers than the polymer spacer (usually 20–100 nm thick) since the plasmon coupling decays exponentially with the spacing distance.[36–38] In addition, the atomic smoothness of *h*-BN films coupled with a low density of dangling points[5,7] maintains the pristine property of graphene layers.

3. Conclusions

In summary, we have successfully synthesized wafer scale, few-layer *h*-BN films by RF plasma chemical vapor depositions

and utilized these as large area dielectric layers on graphene. Tunable plasmon resonances in far-infrared region were demonstrated using lithographically patterned graphene/*h*-BN multistack array. Atomically thin and highly transparent *h*-BN films enable strong plasmon coupling between adjacent graphene layers in the vertical stacks, which produces a significant upshift of the plasmon resonance frequency and magnitude with increasing thickness of the graphene/*h*-BN stacks. This work opens up new possibilities for the applications of graphene/*h*-BN heterostructures in various terahertz photonic devices such as photodetectors, modulators, polarizers, and plasmonics.

4. Experimental Section

RF Plasma CVD Synthesis of the h-BN Films: The synthesis of *h*-BN films was carried out in a remote-discharged, radio frequency (13.56 MHz) plasma chemical vapor deposition (CVD) system. Pure borazine ($B_3N_3H_6$) vapor was used as precursor source for *h*-BN film synthesis. In the growth, a 2-inch Cu (500 nm)/SiO_2/Si wafer was loaded in the CVD chamber and annealed first at 800 °C (ramping rate: 15 °C min^{-1}) for 30 min in hydrogen atmosphere under pressure of 1×10^{-4} Torr. After that, hydrogen gas was cut off and borazine was dosed by a precision leak valve. The growth was initiated by igniting the plasma. During the growth process, the pressure was kept at 4×10^{-5} Torr, a plasma power of 200 W was applied with a substrate table rotating rate of 3 rpm. Finally, after the main growth, the gas flow was cut off and the chamber was cooled down to room temperature under high vacuum.

FTIR Measurements: For plasmonic study, Bruker Vertex 80V FTIR system covering both mid-IR (400 to 7500 cm^{-1}) and far-IR (40 to 700 cm^{-1}) regimes, was used for the transmittance measurements. Corresponding to the mid-IR and far-IR characterizations, liquid nitrogen cooled mercury-cadmium-telluride (MCT) detector and a far-IR deuterated triglycine sulfate (DTGS) detector were used in conjunction with potassium bromide (KBr) and polyethylene terephthalate (PET) beam splitters, respectively. All the measurements were carried out under vacuum at room temperature.

Supporting Information

Supporting Information is available from the Wiley Online Library or from the author.

Acknowledgements

National Research Foundation CRP award "Nonlinear Plasmonics to Overcome the Conventional Limit (NRF2012NRF-CRP002–038)" as well as "Novel 2D materials with tailored properties: beyond graphene (NRF2010NRF-CRP001–087)" are kindly acknowledged for supporting this research.

Received: June 12, 2013
Revised: July 20, 2013
Published online: September 1, 2013

[1] K. S. Novoselov, A. K. Geim, S. V. Morozov, D. Jiang, Y. Zhang, S. V. Dubonos, I. V. Grigorieva, A. A. Firsov, *Science* **2004**, *306*, 666.

[2] A. K. Geim, K. S. Novoselov, *Nat. Mater.* **2007**, *6*, 183.

[3] Y. Zhou, Q. L. Bao, B. Varghese, L. Tang, C. H. Sow, K. P. Loh, *Advanced Material* **2010**, *22*, 67.

[4] A. Catellani, M. Posternak, A. Baldereschi, A. J. Freeman, *Phys. Rev. B* **1987**, *36*, 6105.

[5] C. R. Dean, A. F. Young, I. Meric, C. Lee, L. Wang, S. Sorgenfrei, K. Watanabe, T. Taniguchi, P. Kim, K. L. Shepard, J. Hone, *Nat. Nanotechnol.* **2010**, *5*, 722.

[6] H. Wang, T. Taychatanapat, A. Hsu, K. Watanabe, T. Taniguchi, P. Jarillo-Herrero, T. Palacios, *IEEE Electron Device Lett.* **2011**, *32*, 1209.

[7] J. M. Xue, J. Sanchez-Yamagishi, D. Bulmash, P. Jacquod, A. Deshpande, K. Watanabe, T. Taniguchi, P. Jarillo-Herrero, B. J. Leroy, *Nat. Mater.* **2011**, *10*, 282.

[8] L. Britnell, R. V. Gorbachev, R. Jalil, B. D. Belle, F. Schedin, A. Mishchenko, T. Georgiou, M. I. Katsnelson, L. Eaves, S. V. Morozov, N. M. R. Peres, J. Leist, A. K. Geim, K. S. Novoselov, L. A. Ponomarenko, *Science* **2012**, *335*, 947.

[9] S. J. Haigh, A. Gholinia, R. Jalil, S. Romani, L. Britnell, D. C. Elias, K. S. Novoselov, L. A. Ponomarenko, A. K. Geim, R. Gorbachev, *Nat. Mater.* **2012**, *11*, 764.

[10] M. Yankowitz, J. M. Xue, D. Cormode, J. D. Sanchez-Yamagishi, K. Watanabe, T. Taniguchi, P. Jarillo-Herrero, P. Jacquod, B. J. LeRoy, *Nat. Phys.* **2012**, *8*, 382.

[11] E. Rokuta, Y. Hasegawa, K. Suzuki, Y. Gamou, C. Oshima, A. Nagashima, *Phys. Rev. Lett.* **1997**, *79*, 4609.

[12] W. Auwarter, T. J. Kreutz, T. Greber, J. Osterwalder, *Surf. Sci.* **1999**, *429*, 229.

[13] W. Auwarter, H. U. Suter, H. Sachdev, T. Greber, *Chem. Mat.* **2004**, *16*, 343.

[14] F. Muller, K. Stowe, H. Sachdev, *Chem. Mat.* **2005**, *17*, 3464.

[15] F. Mueller, S. Huefner, H. Sachdev, R. Laskowski, P. Blaha, K. Schwarz, *Phys. Rev. B* **2010**, *82*, 113406.

[16] F. Orlando, R. Larciprete, P. Lacovig, I. Boscarato, A. Baraldi, S. Lizzit, *J. Phys. Chem. C* **2012**, *116*, 157.

[17] Y. M. Shi, C. Hamsen, X. T. Jia, K. K. Kim, A. Reina, M. Hofmann, A. L. Hsu, K. Zhang, H. N. Li, Z. Y. Juang, M. S. Dresselhaus, L. J. Li, J. Kong, *Nano Lett.* **2010**, *10*, 4134.

[18] L. Song, L. J. Ci, H. Lu, P. B. Sorokin, C. H. Jin, J. Ni, A. G. Kvashnin, D. G. Kvashnin, J. Lou, B. I. Yakobson, P. M. Ajayan, *Nano Lett.* **2010**, *10*, 3209.

[19] A. Ismach, H. Chou, D. A. Ferrer, Y. P. Wu, S. McDonnell, H. C. Floresca, A. Covacevich, C. Pope, R. Piner, M. J. Kim, R. M. Wallace, L. Colombo, R. S. Ruoff, *ACS Nano* **2012**, *6*, 6378.

[20] K. K. Kim, A. Hsu, X. T. Jia, S. M. Kim, Y. M. Shi, M. Dresselhaus, T. Palacios, J. Kong, *ACS Nano* **2012**, *6*, 8583.

[21] K. K. Kim, A. Hsu, X. T. Jia, S. M. Kim, Y. S. Shi, M. Hofmann, D. Nezich, J. F. Rodriguez-Nieva, M. Dresselhaus, T. Palacios, J. Kong, *Nano Lett.* **2012**, *12*, 161.

[22] K. H. Lee, H. J. Shin, J. Lee, I. Y. Lee, G. H. Kim, J. Y. Choi, S. W. Kim, *Nano Lett.* **2012**, *12*, 714.

[23] A. Reina, X. T. Jia, J. Ho, D. Nezich, H. B. Son, V. Bulovic, M. S. Dresselhaus, J. Kong, *Nano Lett.* **2009**, *9*, 30.

[24] T. Tanaka, A. Itoh, K. Yamashita, E. Rokuta, C. Oshima, *Surf. Rev. Lett.* **2003**, *10*, 697.

[25] P. Lauffer, K. V. Emtsev, R. Graupner, T. Seyller, L. Ley, S. A. Reshanov, H. B. Weber, *Phys. Rev. B* **2008**, *77*, 155426.

[26] Z. W. Peng, Z. Yan, Z. Z. Sun, J. M. Tour, *ACS Nano* **2011**, *5*, 8241.

[27] Z. Yan, Z. W. Peng, Z. Z. Sun, J. Yao, Y. Zhu, Z. Liu, P. M. Ajayan, J. M. Tour, *ACS Nano* **2011**, *5*, 8187.

[28] Z. Q. Li, E. A. Henriksen, Z. Jiang, Z. Hao, M. C. Martin, P. Kim, H. L. Stormer, D. N. Basov, *Nat. Phys.* **2008**, *4*, 532.

[29] H. G. Yan, F. N. Xia, W. J. Zhu, M. Freitag, C. Dimitrakopoulos, A. A. Bol, G. Tulevski, P. Avouris, *ACS Nano* **2011**, *5*, 9854.

[30] L. Ju, B. S. Geng, J. Horng, C. Girit, M. Martin, Z. Hao, H. A. Bechtel, X. G. Liang, A. Zettl, Y. R. Shen, F. Wang, *Nat. Nanotechnol.* **2011**, *6*, 630.
[31] N. M. R. Peres, *Rev. Mod. Phys.* **2010**, *82*, 2673.
[32] A. Das, S. Pisana, B. Chakraborty, S. Piscanec, S. K. Saha, U. V. Waghmare, K. S. Novoselov, H. R. Krishnamurthy, A. K. Geim, A. C. Ferrari, A. K. Sood, *Nat. Nanotechnol.* **2008**, *3*, 210.
[33] H. Medina, Y. C. Lin, D. Obergfell, P. W. Chiu, *Adv. Funct. Mater.* **2011**, *21*, 2687.
[34] H. G. Yan, X. S. Li, B. Chandra, G. Tulevski, Y. Q. Wu, M. Freitag, W. J. Zhu, P. Avouris, F. N. Xia, *Nat. Nanotechnol.* **2012**, *7*, 330.
[35] S. H. Abedinpour, G. Vignale, A. Principi, M. Polini, W. K. Tse, A. H. MacDonald, *Phys. Rev. B* **2011**, *84*, 045429.
[36] H. Yockell-Lelievre, D. Gingras, R. Vallee, A. M. Ritcey, *J. Phys. Chem. C* **2009**, *113*, 21293.
[37] N. Liu, H. Giessen, *Angew. Chem. Int. Ed.* **2010**, *49*, 9838.
[38] N. J. Halas, S. Lal, W. S. Chang, S. Link, P. Nordlander, *Chem. Rev.* **2011**, *111*, 3913.